



Operando X-ray absorption spectroscopic investigation of electrocatalysts state in anion exchange membrane fuel cells

Received: 5 August 2024

Qihao Li¹, Christopher J. Pollock^{1,2}, Joesene Soto^{1,3}, Andrés Molina Villarino¹, Zixiao Shi¹, Mihail R. Krumov¹, David A. Muller^{1,3,4} & Héctor D. Abruna^{1,3}

Accepted: 14 February 2025

Published online: 27 March 2025

Check for updates

Capturing the active state of (electro)catalysts under operating conditions, namely *operando*, is the ultimate objective of (electro)catalyst characterization, enabling the unraveling of reaction mechanisms and advancing (electro)catalyst development. *Operando* insights advance our understanding of the correlations between electrochemical tests and device-level performances.

However, *operando* characterization of electrocatalysts is challenging due to the complexity of electrochemical devices and instrumental limitations. As a result, the majority of electrocatalyst characterizations have been limited to half-cell *in situ* studies. Here, we present an *operando* X-ray absorption spectroscopic study of Mn spinel oxide electrocatalysts in an operating fuel cell employing a custom-designed cell. Our results reveal that in anion exchange membrane fuel cells, the Mn valence state, within spinel Mn_3O_4/C , increases to above 3+, adopting an octahedral coordination devoid of Jahn-Teller distortions. This structural change results in an AEMFC performance equivalent to that of $Co_{1.5}Mn_{1.5}O_4/C$, a composition that outperforms Mn_3O_4/C in rotating disk electrode tests. Our results underscore the importance of *operando* characterizations in elucidating the active state of electrocatalysts and understanding the correlation(s) between electrochemical tests and device performance.

A comprehensive and detailed compositional and structural characterization of electrocatalysts is paramount for gaining insights into electrocatalytic processes and advancing the development of electrocatalysts for electrochemical energy conversion devices^{1,2}. Conventional off-reaction site (*ex-situ*) characterizations of electrocatalysts can provide a fundamental level of understanding of initial and final states/conditions³. However, electrocatalytic processes are not state functions. Electrocatalysts often undergo surface/bulk reconstructions, as well as compositional changes, under operating conditions^{4,5}. Thus, electrocatalyst characterization under reaction-resembling conditions is essential for achieving a true understanding

of the chemical processes involved. Numerous *in-situ* characterization techniques have been successfully developed in recent times, yielding valuable insights despite deviations from optimal reaction conditions (e.g., temperature and pressure) due to instrumental and/or experimental limitations^{6–10}. *In-situ* characterizations usually resemble the conditions of electrochemical tests conducted in the typical three-electrode electrochemical cell, such as rotating disk electrode (RDE) voltammetry tests. Advancing beyond these conditions, to the direct characterization under device-relevant operating conditions (*operando*), can offer precise and valuable insights into the active states of electrocatalysts.

¹Department of Chemistry and Chemical Biology, Cornell University, Ithaca, NY 14853, USA. ²Cornell High Energy Synchrotron Source, Wilson Laboratory, Cornell University, Ithaca, NY 14853, USA. ³Kavli Institute at Cornell (KIC) for Nanoscale Science, Cornell University, Ithaca, NY 14853, USA. ⁴School of Applied and Engineering Physics, Cornell University, Ithaca, NY 14853, USA. e-mail: hda1@cornell.edu

In state-of-the-art fuel cells and water electrolyzers, a membrane electrode assembly (MEA) is employed using polymer electrolytes and ionomers to achieve high power density and device efficiency^{11,12}. The significant differences in experimental conditions (e.g., temperature, electrolyte, pressure) prevent a precise translation of RDE results to MEA device performance¹³. These discrepancies can be quite pronounced for non-precious metal electrocatalysts since their bulk/surface composition/state, can be more environmentally sensitive than that of precious metals^{14,15}. For example, in RDE tests, a Co-Mn/C composite spinel oxide showed far inferior oxygen reduction reaction (ORR) performance when compared to Pt/C (50 mV lower in halfwave potential $E_{1/2}$). However, it achieved a comparable, and even higher performance than Pt/C, at low relative humidity, when tested in anion exchange membrane fuel cells (AEMFCs)¹⁶. As this example illustrates, *operando* characterizations are essential to bridge the knowledge gap between RDE testing and MEA device performance. This enables a more precise assessment of electrocatalyst activity and provides a deeper understanding of the electrochemical catalytic processes involved.

Operando fuel cell characterization can require considerably more complex cell designs due to the intricate nature of electrochemical devices, and the limitations of instruments such as the requirement of low operating pressures and short/shallow probing/sampling depths. Moreover, a sufficient penetration depth is imperative, as the signal must traverse through all components of fuel cell¹⁷. These aspects have made device-level *operando* characterization of fuel cells challenging and rare^{18,19}. In this study, we developed a custom-designed fuel cell device (Fig. 1) for the *operando* X-ray absorption spectroscopy (XAS) study, in fluorescence mode, of electrocatalysts. The cell is comprised of a conventional fuel cell flow field and current collector on one side, and a titanium flow field plate, featuring an X-ray window, on the opposite side. This plate also serves as a current collector. Using synchrotron-based X-rays, we performed an *operando* XAS study of spinel oxide ORR electrocatalysts and captured/monitored applied potential dependent changes in the catalyst metal center valence and coordination in an operating AEMFC. We found that in the AEMFC, the tetragonal Mn_3O_4 spinel nanocrystals transformed/converted to a structure with Mn occupying octahedral sites devoid of Jahn-Teller distortions, and that the average Mn valence state increased to above 3+. This structural transformation resulted in Mn_3O_4/C performing at the same level as $Co_{1.5}Mn_{1.5}O_4/C$ in the AEMFC, while its performance in RDE tests, where tetrahedral Mn^{2+} sites are present, was significantly lower. Our findings strongly suggest that octahedrally coordinated Mn^{3+} sites are more active than tetrahedral sites towards the ORR in alkaline media. This work demonstrates and illustrates the ability of *operando* XAS characterization to capture/identify the active state of electrocatalysts and help in the understanding the electrochemical catalytic processes in detail. They also help inform and direct the design of more active electrocatalysts.

Results and discussion

Structural characterization of spinel oxide electrocatalysts

Spinel oxide Mn_3O_4 , Co_3O_4 , and $Co_{1.5}Mn_{1.5}O_4$ nanocrystals supported on carbon (Mn_3O_4/C , Co_3O_4/C , and $Co_{1.5}Mn_{1.5}O_4/C$, respectively) were synthesized using a simple colloidal approach (see “Methods” for details). The nanocrystal loading on carbon was controlled to be 40 wt % and verified using thermogravimetric analysis (TGA) as shown in Supplementary Fig. 1. Powder X-ray diffraction (PXRD) tests showed that the Co_3O_4/C and the $Co_{1.5}Mn_{1.5}O_4/C$ were single phase and possessed a cubic spinel structure, whereas the Mn_3O_4/C exhibited a tetragonal spinel structure with Jahn-Teller distortion (Supplementary Fig. 2). The domain sizes were calculated to be 5.5 nm for Co_3O_4/C , 7.7 nm for Mn_3O_4/C , and 3.3 nm for $Co_{1.5}Mn_{1.5}O_4/C$ using the Scherrer formula. The structure and particle sizes were further characterized by high-angle annular dark-field scanning transmission electron

microscopy (HAADF-STEM). The Co_3O_4/C exhibited a particle size of around 5 nm (Supplementary Fig. 3) while the Mn_3O_4/C exhibited a slightly larger particle size of around 8 nm (Supplementary Fig. 4). The atomic-scale HAADF-STEM imaging of both Co_3O_4/C and Mn_3O_4/C confirmed a good match with the theoretical structure in terms of symmetry and distances (Supplementary Fig. 3b, 4b inset). $Co_{1.5}Mn_{1.5}O_4/C$ exhibited a particle size of around 4 nm (Supplementary Fig. 5a). In addition, electron energy loss spectroscopy (EELS) elemental mapping revealed a homogeneous distribution of manganese and cobalt (Supplementary Fig. 5b–e).

RDE and AEMFC performance tests

The ORR activity of the spinel oxide electrocatalysts was first evaluated using the conventional RDE method. ORR polarization curves, including both positive and negative-going scans were acquired and corrected for background currents using scans under an Ar-saturated atmosphere (Supplementary Figs. 6–8). Co_3O_4/C exhibited a half-wave potential ($E_{1/2}$) of 0.85 V (vs. RHE) and an onset potential of around 0.91 V (vs. RHE), while Mn_3O_4/C displayed a hysteresis in the ORR polarization curve, with an onset potential of 0.95 V (vs. RHE) in the negative scan and 0.91 V (vs. RHE) in the positive scan (Fig. 2a). However, $Co_{1.5}Mn_{1.5}O_4/C$ exhibited an $E_{1/2}$ of (0.9 V vs. RHE) and an onset potential of 0.95 V vs. RHE in both scan directions (Fig. 2a). The Tafel plots revealed that over the narrow polarization region (≥ 0.88 V vs. RHE), the ORR potential of Mn_3O_4/C was consistently ca. 40 mV lower during the positive scan, at the same kinetic current, when compared to $Co_{1.5}Mn_{1.5}O_4/C$. Moreover, the Tafel slope for Mn_3O_4/C increased from 35 mV/dec to 200 mV/dec as the potential decreased below 0.85 V vs. RHE, while $Co_{1.5}Mn_{1.5}O_4/C$ maintained a Tafel slope of 35 mV/dec and a consistent kinetic current in both potential scan directions (Fig. 2b). The electron transfer numbers, calculated from Levich plots at limiting current density potentials (Fig. 2c) for Mn_3O_4/C and $Co_{1.5}Mn_{1.5}O_4/C$ were 3.6 and 4.0, respectively. The RDE testing results indicated that the addition of cobalt to the spinel oxide boosted the overall ORR activity, resulting in $Co_{1.5}Mn_{1.5}O_4/C$ exhibiting both a higher ORR onset potential and faster kinetics, when compared to Mn_3O_4/C . The cyclic voltammetric (CV) profiles in Ar-saturated KOH showed that the redox couple ascribed to Mn^{2+}/Mn^{3+} at around 0.85 V (vs. RHE) exhibited improved reversibility in $Co_{1.5}Mn_{1.5}O_4/C$ relative to Mn_3O_4/C . The peak-to-peak separation (ΔE_p), at a sweep rate of 50 mV/s, decreased from 130 mV to 80 mV, and the oxidation peak shifted 60 mV negatively (Supplementary Fig. 9a). At a lower scan rate (10 mV/s), a reduction peak at 0.75 V (vs. RHE) was observed for Mn_3O_4/C (Supplementary Fig. 9b). Previous studies have suggested that Mn serves as the active center that binds O_2 during the ORR catalysis process^{16,20}. The change in the Mn redox couple behavior and the disappearance of the hysteresis in the ORR profile suggest that the state of Mn could be a main/dominant factor in determining ORR activity.

The primary objective of the RDE test was to assess the activity of the electrocatalysts and predict their performance in practical devices. To establish/validate the correlation between RDE testing and device-level performance in a fuel cell, we conducted AEMFC tests for Mn_3O_4/C and $Co_{1.5}Mn_{1.5}O_4/C$. The AEMFC performance was recorded in a constant current mode from maximum current density to open circuit potential (OCP), corresponding to a positive scan in RDE testing. It was anticipated that Mn_3O_4/C would exhibit a lower peak power density (PPD) and OCP compared to $Co_{1.5}Mn_{1.5}O_4/C$, owing to its lower onset potential and slower ORR kinetics exhibited in the RDE tests. Surprisingly, both Mn_3O_4/C and $Co_{1.5}Mn_{1.5}O_4/C$ displayed an equally impressive performance in the AEMFC device test. At a loading of 1.2 mg cm⁻², both exhibited a PPD of 1.5 W cm⁻², a maximum current density of 3.5 A cm⁻², and an OCP of 0.95 V (Fig. 2d). At a reduced/lower loading of 0.8 mg cm⁻², both electrocatalysts also achieved similar PPDs of 1.2 W cm⁻² and OCPs of 0.95 V (Supplementary Fig. 10). Both Mn_3O_4/C and $Co_{1.5}Mn_{1.5}O_4/C$ exhibited the same structure after AEMFC tests, as verified by atomic-scale

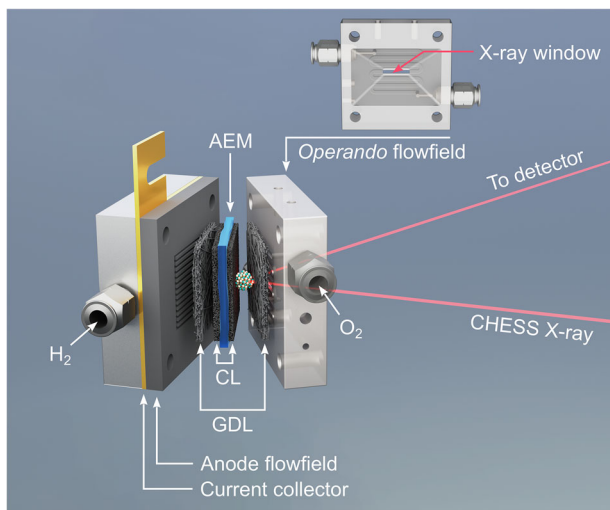


Fig. 1 | Schematic diagram of the design of *operando* X-ray absorption spectroscopy (XAS) fuel cell device. The anode (left) side features a conventional single-cell configuration with a graphite flow field and a gold-coated copper current collector. The cathode (right) side is an *operando* Ti flow field with an X-ray window for fluorescence-mode XAS measurements (sealed with Kapton film during XAS measurement). A 5-layer anion exchange membrane fuel cell (AEMFC) MEA with catalysts layer (CL) and carbon paper gas diffusion layer (GDL), same as a single cell test setup, is sandwiched in between the flow field plates (gaskets are omitted for clarity). The cell temperature is controlled with a silicone rubber heater using a temperature probe and humidified H₂ and O₂ are supplied using a fuel cell humidification system.

HAADF-STEM images (Supplementary Fig. 11, 12a). Mn and Co maintained a homogeneous distribution, as shown in EELS elemental mapping (Supplementary Fig. 12b-d). The disparity observed between the RDE and AEMFC testing results suggests that differences in the testing environments may have led to changes in the spinel electrocatalysts, potentially/likely associated with the Mn sites.

In-situ and *operando* XAS study

In-situ and *operando* XAS measurements were conducted to study the states of the Mn spinel ORR electrocatalysts and to understand the discrepancy between the RDE and AEMFC results. In-situ XAS measurements were conducted using a previously reported custom-design electrochemical cell²¹ (see “Methods” for details). CV profiles obtained using the in-situ cell, exhibited the same features as those in regular RDE tests (Supplementary Fig. 13). X-ray absorption near edge structure (XANES) spectra indicated that the Mn in Co_{1.5}Mn_{1.5}O₄/C exhibits a higher valence oxidation state when compared with Mn₃O₄/C (Supplementary Fig. 14a). Fourier-transformed extended X-ray absorption fine structure (FT-EXAFS) data (without phase correction) displayed a first shell peak at R + Δ of 1.4 Å for both Mn₃O₄/C and Co_{1.5}Mn_{1.5}O₄/C, corresponding to a Mn-O bond (Supplementary Fig. 14b). Co_{1.5}Mn_{1.5}O₄/C displayed a second shell peak at R + Δ of 2.5 Å corresponding to edge-sharing octahedral metal sites (M_{oct}-M_{oct}), while the second shell of Mn₃O₄/C split into two peaks (R + Δ of 2.3 Å and 2.8 Å) due to Jahn-Teller distortions (Supplementary Fig. 14b), corresponding to parallel (//) and perpendicular (⊥) edge-sharing octahedral metal sites as illustrated in Supplementary Fig. 15. The in-situ XANES spectra of Mn₃O₄/C exhibited a systematic shift in the edge position with applied potential, notably exhibiting a significant decrease (0.5 eV) in the edge energy when the applied potential was changed from 1.0 V to 0.8 V vs. RHE; the potential range coinciding with the observed ORR

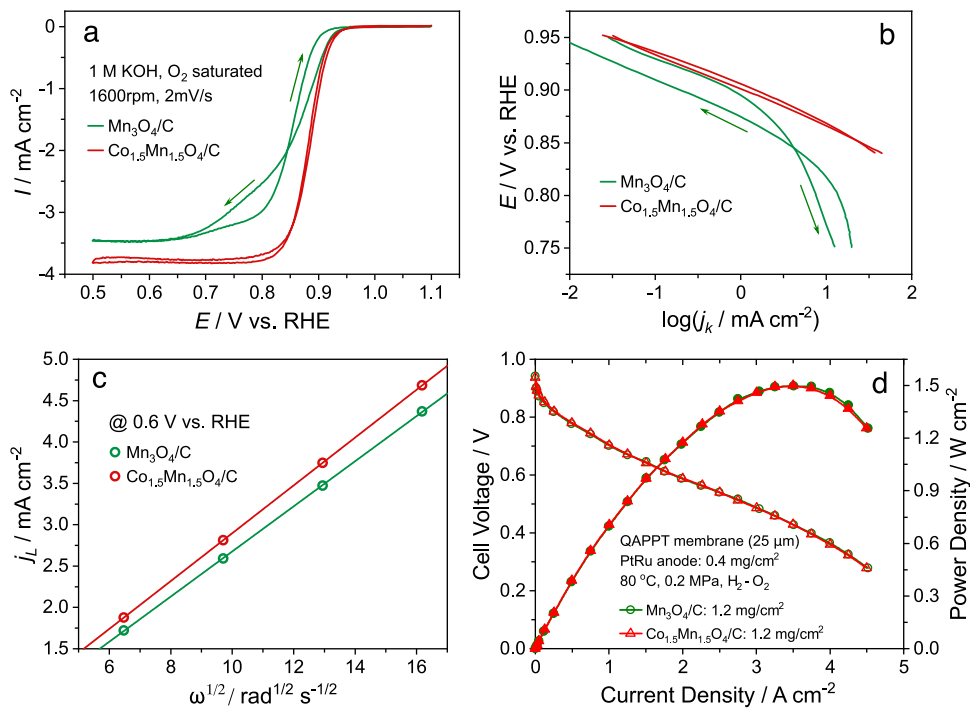


Fig. 2 | Rotating disk electrode (RDE) and AEMFC tests of Mn₃O₄/C (green) and Co_{1.5}Mn_{1.5}O₄/C (red) catalysts. **a** Background subtracted oxygen reduction reaction (ORR) polarization curve in O₂ saturated 1 M KOH at 1,600 rpm rotation speed and 2 mV/s scan rate and corresponding. **b** Tafel plots of kinetic current (j_k) with arrows indicating polarization scan directions. **c** Levich plots and corresponding

linear fitting over the limiting current density (j_L) region (0.6 V vs. RHE) at different electrode rotating rate (ω). **d** H₂-O₂ AEMFC performance of Mn₃O₄/C (green circle) and Co_{1.5}Mn_{1.5}O₄/C (red triangle) paired with PtRu/C anode (0.4 mg/cm²) at 80 °C with 0.2 MPa backpressure.

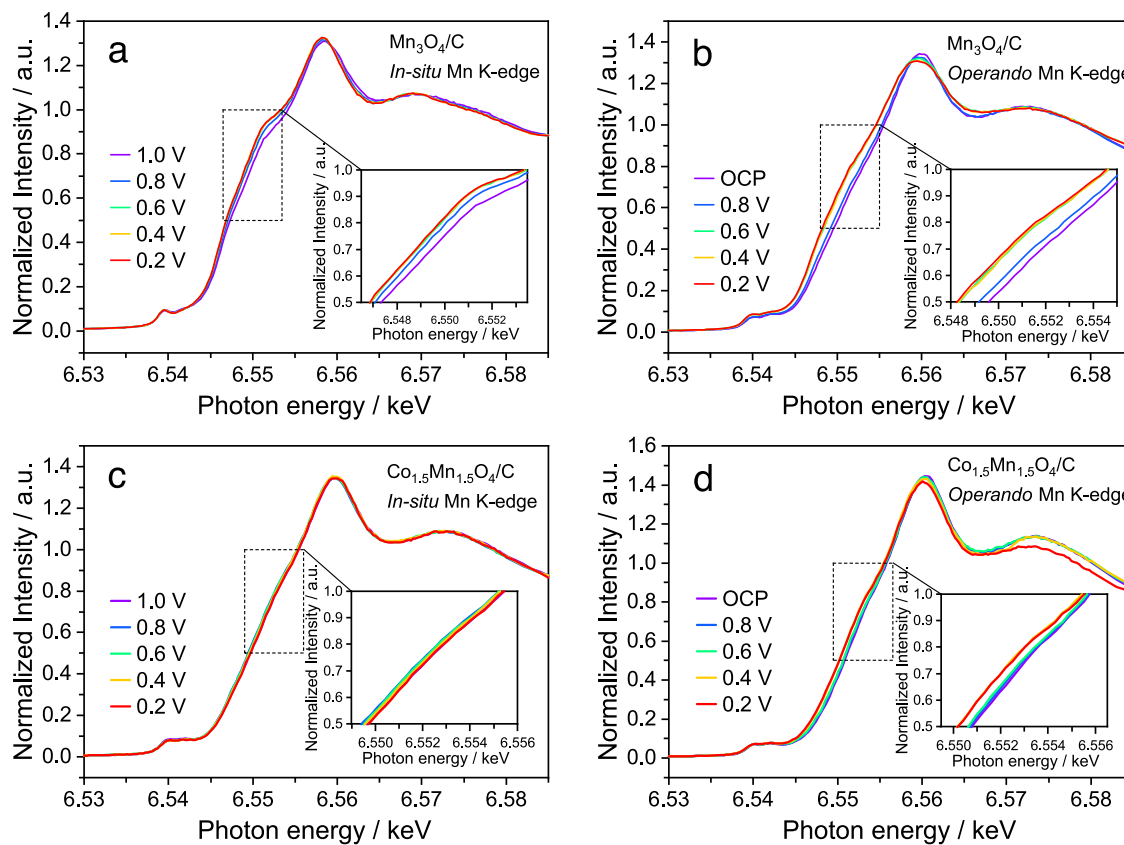


Fig. 3 | In-situ and operando Mn K-edge X-ray absorption near edge structure (XANES) spectra of catalysts. In situ Mn K-edge XANES spectra of (a) $\text{Mn}_3\text{O}_4/\text{C}$ and (c) $\text{Co}_{1.5}\text{Mn}_{1.5}\text{O}_4/\text{C}$ at potentials ranging from 1.0 V to 0.2 V (vs. RHE). AEMFC

Operando Mn K-edge XANES spectra of (b) $\text{Mn}_3\text{O}_4/\text{C}$ and (d) $\text{Co}_{1.5}\text{Mn}_{1.5}\text{O}_4/\text{C}$ at OCP and cell voltages ranging from 0.8 V to 0.2 V. Insets show the expanded edge section of intensity ranging from 0.5 to 1.0.

hysteresis (Fig. 3a). In contrast, $\text{Co}_{1.5}\text{Mn}_{1.5}\text{O}_4/\text{C}$ exhibited a minimal shift in the edge energy with applied potential (Fig. 3c). Additionally, its average edge energy was about 3 eV higher than that of $\text{Mn}_3\text{O}_4/\text{C}$ (Supplementary Fig. 16), indicating a higher valence/oxidation state. These in-situ XANES findings are consistent with the hypothesis that the Mn oxidation state plays a pivotal role in influencing the ORR performance and suggest that Mn in a 3+ valence state, exhibits enhanced ORR activity.

Operando XAS experiments were further conducted to reveal the correlation between ORR performance and the states of the Mn spinel oxide electrocatalysts under AEMFC operating conditions. The high transmission/penetration of hard X-rays through the gas diffusion layer (GDL) carbon paper, as shown by the calculated result in Supplementary Fig. 17²², enabled XAS measurements of a complete AEMFC device using our home-designed and built *operando* cell (see “Methods” for details). Due to safety considerations at the synchrotron station, AEMFCs were tested at 60 °C with a gas flow rate of 200 sccm without additional backpressure. Nevertheless, $\text{Mn}_3\text{O}_4/\text{C}$ and $\text{Co}_{1.5}\text{Mn}_{1.5}\text{O}_4/\text{C}$ demonstrated similar performance under operando XAS measurement conditions (Supplementary Fig. 18), suggesting that the discrepancy between RDE and AEMFC testing persists under these conditions. The *operando* XANES spectra of $\text{Mn}_3\text{O}_4/\text{C}$ also showed a systematic edge energy shift with cell voltage, revealing a 1 eV decrease in edge energy position when the applied potential was changed from 0.8 V to 0.2 V (Fig. 3b). However, it is noteworthy that the edge energy was approximately 2 eV higher when compared to its in-situ XANES spectra (Supplementary Fig. 19), indicating a much higher Mn oxidation state under *operando* conditions. This edge energy shift was observed when temperature and O_2 gas were applied to the AEMFC (Supplementary Fig. 20), indicating that the Mn state change is primarily driven by the more oxidative environment in AEMFCs. In

contrast, the *operando* XANES spectra of $\text{Co}_{1.5}\text{Mn}_{1.5}\text{O}_4/\text{C}$ displayed an edge energy that was nearly identical to the in-situ XANES spectra (Supplementary Fig. 21), with only a slight increase in the edge energy shift in response to changes in the applied potential (Fig. 3d). The *operando* XANES spectra revealed that $\text{Mn}_3\text{O}_4/\text{C}$ exhibited an edge energy that was very similar to that of $\text{Co}_{1.5}\text{Mn}_{1.5}\text{O}_4/\text{C}$ in AEMFCs. The observed changes of the electrocatalysts, from in-situ to *operando* conditions, coincide with the discrepancy observed between the RDE and AEMFC testing results. This observation further emphasizes the pivotal role of Mn oxidation states in determining the ORR activity of Mn spinel-based electrocatalysts.

For a detailed analysis of the in-situ and *operando* XANES data, the average valence states of Mn were extracted from XANES edge energy values (see “Methods”). A strong linear relationship between the edge energy and the valence state was observed for reference manganese oxide samples as shown in Supplementary Fig. 22. Since the species being studied here also consist of high spin Mn, exclusively coordinated by oxygen-derived ligands, we feel confident that this correlation can thus be used to estimate the effective oxidation state of Mn in these samples. Correspondingly, the determined/derived Mn valence states of $\text{Mn}_3\text{O}_4/\text{C}$ and $\text{Co}_{1.5}\text{Mn}_{1.5}\text{O}_4/\text{C}$ under different conditions are presented in Fig. 4a. Under ex-situ conditions, $\text{Mn}_3\text{O}_4/\text{C}$ exhibited an average Mn valence state of 2.7+, which corresponds to the characteristic value of a standard spinel with a 1:2 ratio between 2+ tetrahedral sites and 3+ octahedral sites. Conversely, $\text{Co}_{1.5}\text{Mn}_{1.5}\text{O}_4/\text{C}$ exhibited an average Mn valence state of 3.1+, suggesting Mn occupation primarily at octahedral sites. Under in-situ electrochemical conditions, the average Mn valence state of $\text{Mn}_3\text{O}_4/\text{C}$ varied from 2.6+ to 2.8+, while the average Mn valence state of $\text{Co}_{1.5}\text{Mn}_{1.5}\text{O}_4/\text{C}$ was unchanged at 3.3+. The much higher oxidation state of Mn in $\text{Co}_{1.5}\text{Mn}_{1.5}\text{O}_4/\text{C}$ under ex-situ and in-situ conditions is due to the

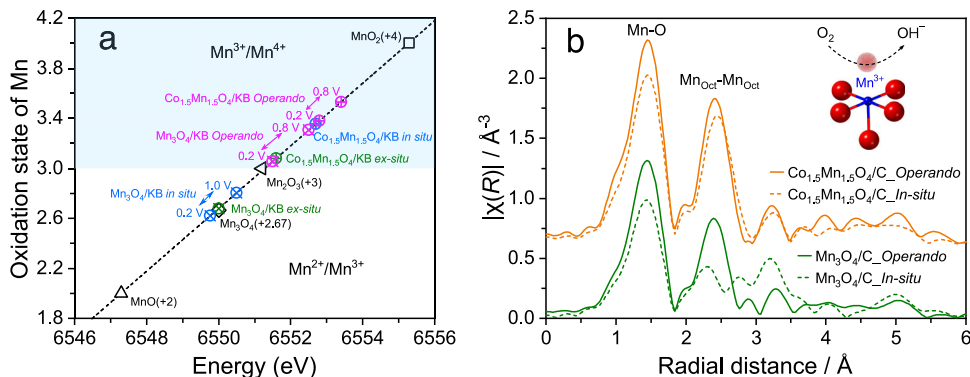


Fig. 4 | Determination of Mn oxidation state and coordination environment. **a** Average Mn oxidation state of $\text{Mn}_3\text{O}_4/\text{C}$ and $\text{Co}_{1.5}\text{Mn}_{1.5}\text{O}_4/\text{C}$ under ex-situ, in-situ and *operando* conditions, determined from the Mn edge energy using MnO , Mn_3O_4 , Mn_2O_3 , and MnO_2 as standards. **b** In situ (dash line) and *Operando* (solid line) Mn K

edge k^2 -weighted Fourier transformed extended X-ray absorption fine structure (FT-EXAFS) data (without phase correction) of $\text{Mn}_3\text{O}_4/\text{C}$ (green) and $\text{Co}_{1.5}\text{Mn}_{1.5}\text{O}_4/\text{C}$ (yellow). The inset illustrates the proposed octahedral Mn^{3+} active sites for catalyzing the ORR.

preferential occupation of Co in the 2+ tetrahedral sites, as evidenced by Co K-edge XANES spectra (Supplementary Fig. 23) and the corresponding extracted Co oxidation state (Supplementary Fig. 24). Co exhibited a low oxidation state of +2.2 in $\text{Co}_{1.5}\text{Mn}_{1.5}\text{O}_4/\text{C}$, which increased to +2.3 in RDE tests, compared to the standard +2.67 in Co_3O_4 (Supplementary Fig. 24b). Under *operando* AEMFC conditions, the average Mn valence state of $\text{Co}_{1.5}\text{Mn}_{1.5}\text{O}_4/\text{C}$ varied between 3.4+ to 3.6+. Surprisingly, the average Mn valence state in $\text{Mn}_3\text{O}_4/\text{C}$ increased beyond 3+, ranging from 3.1+ to 3.3+. These changes were expected given the considerably harsher conditions, higher temperatures (60–80 °C vs. room temperature), pure O_2 atmosphere (compared to O_2 dissolved in KOH solution), and current densities (A vs. mA) present under fuel cell operating conditions. The oxidation states of Mn in $\text{Mn}_3\text{O}_4/\text{C}$ and $\text{Co}_{1.5}\text{Mn}_{1.5}\text{O}_4/\text{C}$ at each potential/voltage during in-situ and *operando* tests are shown in Supplementary Fig. 25, showing an increase of oxidation state with potential/voltage. Our analysis of Mn valence states, in conjunction with the RDE and AEMFC testing results, strongly suggest that achieving an average Mn valence state beyond 3+, in other words eliminating Mn^{2+} species, is pivotal for attaining high ORR performance.

The coordination environments of the Mn centers under in-situ and *operando* conditions were further investigated with FT-EXAFS data, as shown in Fig. 4b (raw and k^2 -weighted EXAFS data are shown in Supplementary Fig. 26). Both $\text{Co}_{1.5}\text{Mn}_{1.5}\text{O}_4/\text{C}$ and $\text{Mn}_3\text{O}_4/\text{C}$ showed an increased Mn-O peak ($R + \Delta$ of 1.4 Å) intensity under *operando* conditions, likely due to higher degree of crystallinity in AEMFCs as analyzed above. $\text{Co}_{1.5}\text{Mn}_{1.5}\text{O}_4/\text{C}$ exhibited a similar radial distribution under both in-situ and *operando* conditions, with a slightly shorter second shell ($M_{\text{oct}}\text{-}M_{\text{oct}}$) distance likely due to the contraction induced by the higher Mn valence state. In contrast, $\text{Mn}_3\text{O}_4/\text{C}$ displayed a significantly different radial distribution under *operando* conditions. The second shell peaks merged into a single peak at $R + \Delta$ of 2.4 Å, indicating the formation of a new structure that is devoid of Jahn-Teller distortions. This structure also differs from that of Mn_2O_3 , where the second shell is located at $R + \Delta$ of 2.7 Å (Supplementary Fig. 27). EXAFS data fitting employing a spinel model with tetrahedral and octahedral sites resulted in a poor match (Supplementary Fig. 28a), while fitting using a model with only octahedral sites, resulted in a good match (Supplementary Fig. 28b), strongly suggesting that Mn occupies octahedral sites under *operando* AEMFC conditions. Future work will involve the use of *operando* X-ray diffraction methods to obtain a detailed understanding of the structural changes involved.

The correlation between ORR activity and Mn oxidation state and coordination environment in the spinel could be established through the insights gained from in-situ and *operando* XAS investigations. Mn occupied octahedral sites in $\text{Co}_{1.5}\text{Mn}_{1.5}\text{O}_4/\text{C}$ with an average valence

state above 3+ under both in-situ and *operando* conditions, achieving good performance in both RDE and AEMFC tests. Conversely, $\text{Mn}_3\text{O}_4/\text{C}$, which possesses a tetragonal spinel structure with both tetrahedral Mn^{2+} and octahedral Mn^{3+} sites, exhibited a lower ORR performance in RDE tests. However, the formation of a structure featuring octahedrally coordinated Mn with an average oxidation state above 3+ under *operando* conditions resulted in an AEMFC performance equal to that of $\text{Co}_{1.5}\text{Mn}_{1.5}\text{O}_4/\text{C}$. The increased ORR activity of high-valence-state Mn ($\geq 3+$) suggests that a stronger binding energy with oxygen species/intermediates is advantageous for Mn-based oxides in catalyzing ORR. This finding is consistent with the high H_2O_2 yield observed for $\text{Mn}_3\text{O}_4/\text{C}$ in RDE tests, which show a lower limiting current density (Fig. 2a) and an electron transfer number of 3.6 (Fig. 2c), when low-valence-state Mn^{2+} is present. These results verified the importance of device-level *operando* characterization, especially for non-PGM electrocatalysts as they are more sensitive to environmental conditions, to probe the true active state of electrocatalysts under working conditions. Our findings suggest that Mn^{3+} with octahedral coordination, as depicted in the upper right of Fig. 4b, represents the active site with high ORR activity. Moreover, a short Mn-O⁺ (manganese to reactive oxy-intermediates) distance, free of Jahn-Teller distortions, is likely more favorable for catalyzing the ORR.

To summarize, we have successfully conducted *operando* XAS measurements using a custom-designed cell to elucidate the valence state and coordination environment of Mn spinel oxide electrocatalysts. Our findings suggest that Mn, with a valence state of 3+ or higher and octahedral coordination environment, exhibits high ORR activity. The preferred octahedral occupation of Mn in $\text{Co}_{1.5}\text{Mn}_{1.5}\text{O}_4/\text{C}$ contributes to its high ORR performance in both RDE and AEMFC tests. In contrast, $\text{Mn}_3\text{O}_4/\text{C}$, which initially contained both tetrahedral Mn^{2+} sites and Jahn-Teller distorted octahedral Mn^{3+} sites, transformed into a structure characterized solely by octahedral Mn^{3+} sites in the AEMFC environment. This transformation enabled $\text{Mn}_3\text{O}_4/\text{C}$ to achieve an AEMFC performance comparable to that of $\text{Co}_{1.5}\text{Mn}_{1.5}\text{O}_4/\text{C}$, albeit with considerably lower performance in RDE testing. This work illustrates the importance and necessity of *operando* XAS characterization for revealing the active states of electrocatalysts and understanding electrocatalytic processes.

Methods

Synthesis of carbon supported spinel oxides

Nano-sized spinel oxides supported on carbon were synthesized using a facile ethanol refluxing method. For the synthesis of 40 wt% $\text{Mn}_3\text{O}_4/\text{C}$, 245 mg (1 mmol) of manganese (II) acetate tetrahydrate ($\text{Mn}(\text{CH}_3\text{COO})_2 \cdot 4\text{H}_2\text{O}$, ≥99.0%, Sigma-Aldrich) were dissolved in 150 mL of pure ethanol (≥99.5%, Koptec) and 5 mL ammonium

hydroxide solution (28.0–30.0% NH₃ basis, Sigma-Aldrich) were then added under magnetic stirring. 107 mg of Ketjen Black carbon powder were added and the mixture was sonicated for 30 min to achieve a good dispersion. The mixture was then refluxed for 4 h under continuous magnetic stirring. The product was collected by centrifugation (10 min at 9000 rpm (9056 RCF)) and dried for 24 h at 160 °C in an air oven. 40 wt% Co_{1.5}Mn_{1.5}O₄/C was synthesized in the same manner using 125 mg (0.5 mmol) of cobalt(II) acetate tetrahydrate (Co(CH₃COO)₂·4H₂O, ≥98.0%, Sigma-Aldrich) and 123 mg (0.5 mmol) of manganese(II) acetate tetrahydrate (Mn(CH₃COO)₂·4H₂O, ≥99.0%, Sigma-Aldrich). 40 wt% Co₃O₄/C was synthesized in the same manner using 245 mg (1 mmol) of cobalt(II) acetate tetrahydrate (Co(CH₃COO)₂·4H₂O, ≥98.0%, Sigma-Aldrich). The amount of carbon added was adjusted accordingly to synthesize 60 wt% spinel oxide for AEMFC tests.

Structural and morphological characterization

TGA tests were conducted using a TA Instruments 5500 Thermo-gravimetric Analyzer. The measurements were carried out with an airflow rate of 10 standard cubic centimeters per minute (scm), and the temperature ramp was set at 10 °C/min. PXRD patterns were obtained using a Bruker D8 Advance ECO powder diffractometer equipped with a Cu K α radiation source ($\lambda = 1.5406 \text{ \AA}$). The instrument operated at 1 kW (40 kV and 25 mA), with a step size of 0.01945 degrees and an acquisition time of 0.5 seconds per data point. STEM samples were prepared by applying catalyst suspensions in ethanol onto a lacy carbon TEM grid (Electron Microscopy Science, 200 Mesh, Copper grid). Subsequently, the grids were dried under an Infrared (IR) lamp and then baked in a vacuum chamber ($1.3 \times 10^{-7} \text{ Torr}$) at 120 °C for 12 hours to eliminate surface contaminants. STEM images were acquired utilizing a Thermo Fisher Spectra 300 STEM microscope with an accelerating voltage of 300 kV. The spot size was configured to 9, the C2 aperture was set to 50 μm , and the camera length and converging angle were adjusted to 130 mm and 21.4 mrad, respectively. The EELS spectra were captured with a spot size of 6 and an aperture size of 50 μm . To mitigate the risk of potential beam damage, a dwell time of 2 ms was established for each pixel. Subsequently, the EELS spectra were processed using the Cornell Spectrum Imager (CSI) plugin in ImageJ²³. Background subtraction was carried out using the linear combination of power law (LCPL) method at 50 eV before reaching the edge onset. Elemental mapping was executed utilizing the Co L_{2,3} edge and Mn L_{2,3} edge.

Electrochemical measurements

Electrochemical tests were conducted employing a standard 3-electrode configuration. A glassy carbon (GC) RDE (Pine Instruments, USA) with a 5.5 mm diameter was employed as the working electrode (WE), a carbon rod was utilized as the counter electrode (CE), and a custom-made reversible hydrogen electrode (RHE) served as the reference electrode (RE). All experiments were carried out in 1 M KOH freshly prepared and stored in plastic bottle, and potentials were reported with reference to RHE without any conversion. The catalysts were dispersed in a Nafion/isopropanol solution (0.1 wt%) using ice bath sonication to generate a catalyst ink with a concentration of 5 mg mL⁻¹. Subsequently, 12 μL of the desired catalyst ink were drop-casted onto the GC electrode and dried at a rotation speed of 500 rpm, resulting in a loading of 100 $\mu\text{g cm}^{-2}$. ORR polarization curves were obtained in O₂-saturated 1 M KOH using a WaveDriver 10 potentiostat system (Pine Instruments, USA). The system was equipped with a modulated speed rotator for WE rotation speed control. A scan rate of 2 mV/s was selected to minimize the influence of the double layer capacitance. No iR correction techniques were applied before nor after data acquisition. Kinetic current densities (j_K) of the Tafel plot and the electron transfer numbers were calculated using the Koutecký-Levich

equation:

$$\frac{1}{j} = \frac{1}{j_L} + \frac{1}{j_K} \quad (1)$$

where j is the overall current density and j_L is the diffusion-limited current, which can be expressed as:

$$j_L = 0.62nFAD^{\frac{2}{3}}U^{-\frac{1}{6}}C\omega^{\frac{1}{2}} \quad (2)$$

where n is electron transfer number, F is Faraday's constant, D is the diffusion coefficient of oxygen in 1 M KOH, U is the kinematic viscosity of 1 M KOH, C is the saturated concentration of oxygen in 1 M KOH, and ω is the angular velocity of the electrode. CV profiles were obtained in Ar-saturated 1 M KOH at a scan rate of 50 mV/s or 10 mV/s without rotation. Multiple scans were performed until the CV profiles overlapped.

MEA preparation and AEMFC performance tests

The MEAs were prepared using a custom-built ultrasonic spray system. This system comprised a FocusMist ultrasonic nozzle (Siansonic, China), a Legato 100 Infuse Single syringe pump (KD Scientific, USA), and an HTP-MB1-L18/W18-200 PRF vacuum hot plate (Thermansys, Greece) and a Y&D 7300 gantry robot (Y&D Technology, China) (modified with custom-built parts manufactured by the Cornell Laboratory of Atomic and Solid State Physics (LASSP) Professional Machine Shop) were utilized in the MEA fabrication process. The gantry robot was programmed to execute an orthogonal brush pattern with a line spacing of 1 mm. Previously reported quaternary ammonium poly (N-methyl-piperidine-co-p-terphenyl) (QAPPT) alkaline polymer electrolyte was used as both membrane (20 μm thickness) and ionomer²⁴. During the spraying process, a plastic stencil with a $2 \times 2 \text{ cm}^2$ square opening was employed to cover the QAPPT membrane, thereby defining the active electrode area. The number of spray cycles was determined based on a calibration curve established by spraying a carbon ink onto an aluminum foil to achieve the desired loading. Air was employed as the carrier gas for the ultrasonic nozzle with a flow rate of 4 L min⁻¹. A commercial PtRu/C (60 wt%, Fuel cell store) anode ink was made at a concentration of 10 mg mL⁻¹ and an ionomer content of 22 wt%. Mn₃O₄/C (60 wt%) and Co_{1.5}Mn_{1.5}O₄/C (60 wt%) inks concentrations were set to 20 mg mL⁻¹ and an optimized ionomer content of 19 wt%. In general, the catalyst was mixed with a specific volume of ethanol/isopropanol (1:1) solvent and the QAPPT ionomer solution (80 mg mL⁻¹ in DMSO) in a glass vial to achieve the desired concentration and ionomer content. The mixture was first sonicated using a CPX5800H sonicator (Branson Ultrasonics, USA) in an ice bath for 10 minutes. Subsequently, it was sonicated using a Q125 probe sonicator (Qsonica Sonicators, USA) for 10 minutes at 25% power with 1 s on/off intervals, also in an ice bath. After that, the mixture was shear mixed for 2 minutes at 18,000 rpm using a FILMIX Model 30-L high-speed shear mixer (PRIMIX, Japan). The ink was then sonicated in an ice bath for an additional 5 minutes before being sprayed onto the membrane using the ultrasonic spray system to form the catalyst layer. The temperature of the vacuum hot plate was set to 60 °C. The anode side of the MEAs was applied with 0.4 mg_{metal} cm⁻² of PtRu/C, and the cathode with a spinel oxide loading of 0.8 or 1.2 mg cm⁻². Ion exchange for MEAs was performed in 1 M KOH at 70 °C and the KOH solution was changed four times over a period of 72 hours. The MEA was thoroughly rinsed with deionized water five times to remove residual KOH prior to the fuel cell test.

A single-cell device was assembled using a custom-made fuel cell fixture with a custom-designed flow field pattern. AvCarb 3250 gas diffusion layers (GDLs) and 170 μm PTFE gaskets were used, and the bolt torque was set to 4 N·m. The fuel cell performance was evaluated using an 850 Fuel Cell Test System (Scribner, USA), the cell

temperature was set to 80 °C, and both anode and cathode were operated with 100% relative humidity (RH) and a back pressure of 200 kPa. H₂ and N₂ were flowed in the anode and cathode with a flow rate of 100 sccm, respectively, during the temperature ramp-up process, and the cathode gas was switched to O₂ for test when the cell temperature reached 80 °C. The AEMFC activation was initiated with a small current applied once the cell reached the target temperature, held until no significant increase in cell voltage was observed, and then incrementally increased. This process was continued until the cell voltage dropped below 0.3 V, after which the polarization curve was recorded in constant current mode, sweeping from maximum current to OCP. The gas flow rate was gradually increased during the activation process and finally set to 1500 sccm for both the anode and cathode. No iR correction techniques were employed before or after data acquisition.

In-situ and operando XAS measurements

XAS measurements were conducted in fluorescence mode with a four-element Vortex detector at the PIPOXS beamline of the Cornell High Energy Synchrotron Source (CHESS) under ring conditions of 100 mA and 6 GeV. The incident beam was energy selected using a liquid nitrogen cooled Si(111) monochromator and the beam was 1×2 mm at the sample and harmonic rejection was achieved using a pair of Rh-coated mirrors. Mn K edge spectra were collected from 6.4 to 7.1 keV and were calibrated using the Mn foil absorption K edge at 6539 eV (using the maximum of the first derivative). In-situ electrochemical XAS measurements were conducted using a custom-designed PEEK (polyether ether ketone) electrochemical cell, as described previously²¹. The same catalyst ink employed for AEMFC tests was applied onto a 1×1 cm² area of a carbon paper strip (Avcarb 3250) using the homemade ultrasonic spray system to achieve a loading of 0.8 mg/cm² to maximize signal intensity while also limiting self-absorption, and this region loaded with the catalyst was positioned facing the Kapton film (250 µm) window of the in-situ X-ray electrochemical cell. A carbon rod was used as the CE and an RHE RE was connected to the cell using a Luggin capillary. The cell was filled with 1 M KOH and purged with O₂ during the experiments. XAS spectra were acquired at different potentials, ranging from 1.0 to 0.2 V (vs. RHE) with 0.2 V intervals. Spectra were averaged from 4 scans to improve the signal-to-noise ratio to reach a minimum k value of 11 in FT-EXAFS data. A new spot was used after every 4 scans to ensure no beam damage. A series of nine continuous EXAFS scans conducted on the same spot of the Mn₃O₄/C sample prior to normalization is shown in Supplementary Fig. 29. The spectra show no changes in shape, features, edge energy, or intensity, indicating no evidence of beam damage.

Operando XAS measurements were conducted using the custom-made cell. The flow field, current collector, and endplate were integrated into a single piece, with an X-ray window opening designed to support fluorescence mode XAS measurements. This window has a 2 mm height—matching the serpentine flow field width—and a width of 1 cm, with a 130-degree horizontal opening angle to allow for a 90-degree angle between the incident beam and detector. A 250 µm Kapton film was used to seal the window. MEAs fabricated and ion-exchanged in the same manner as the ones used for AEMFC tests with 0.4 mg_{metal} cm⁻² of PtRu/C anode and 0.8 mg cm⁻² of spinel cathode were used for measurements to maximize signal intensity while also limiting self-absorption. The MEA electrode area was controlled to be 2 cm² (1.4 cm × 1.4 cm) to accommodate the potentiostat current limit. The cell was assembled in the same manner as for the AEMFC tests with the cathode side facing the Kapton film (250 µm) sealed X-ray window. The cell was positioned with the X-ray window at a 45-degree angle relative to both the incident beam and the fluorescence detector. Due to safety regulations in the synchrotron station, the cell temperature

was set at 60 °C during the experiments, and 100% RH H₂ and O₂ gases were supplied to the anode and cathode, respectively, using a humidification system (Fuel Cell Technologies, USA) at a flow rate of 200 sccm without backpressure. The cell potential was controlled using an Interface 5000E potentiostat (Gamry Instruments, USA) with a maximum current of 5 A. XAS spectra were acquired in the same manner at OCP and at potentials ranging from 0.8 to 0.2 V with 0.2 V intervals. The spectra were averaged from 4 scans to improve the signal-to-noise ratio and a new spot was used after every 4 scans.

The reference powder samples including MnO (99%, Sigma-Aldrich), Mn₃O₄ (97%, Sigma-Aldrich), Mn₂O₃ (99%, Sigma-Aldrich), and MnO₂ (99%, Sigma-Aldrich) were ground with boron nitride for dilution and subsequently loaded onto a 1 mm thick aluminum holder with a Kapton film window. Spectra were averaged from 5 scans to improve the signal-to-noise ratio. XAS data were analyzed using the Athena and Artemis software packages²⁵. The correlation between oxidation state and edge energy was established using reference powder samples with the same method as reported previously²⁶. Fourier transformation of EXAFS spectra was performed using a Hanning window from 3 to 11 Å⁻¹ with k² weighting and no phase correction. EXAFS fitting was conducted in the R space with k, k², and k³ weights in the range of 0 to 4 Å⁻¹.

Data availability

The data supporting the findings of this study are included within the article and its Supplementary Information files. Source data are provided with this paper.

References

1. Yang, Y. et al. Operando methods in electrocatalysis. *ACS Catal.* **11**, 1136–1178 (2021).
2. Gourdin, G. & Doan-Nguyen, V. In situ, operando characterization of materials for electrochemical devices. *Cell Rep. Phys. Sci.* **2**, 100660 (2021).
3. Boddula, R. & Asiri, A. M. *Methods for Electrocatalysis: Advanced Materials and Allied Applications*. (Springer, 2020).
4. Zeng, Y. et al. Surface reconstruction of water splitting electrocatalysts. *Adv. Energy Mater.* **12**, 2201713 (2022).
5. Jiang, H., He, Q., Zhang, Y. & Song, L. Structural self-reconstruction of catalysts in electrocatalysis. *Acc. Chem. Res.* **51**, 2968–2977 (2018).
6. Timoshenko, J. & Roldan Cuenya, B. In situ/operando electrocatalyst characterization by X-ray absorption spectroscopy. *Chem. Rev.* **121**, 882–961 (2021).
7. Han, Y., Zhang, H., Yu, Y. & Liu, Z. In situ characterization of catalysis and electrocatalysis using APXPS. *ACS Catal.* **11**, 1464–1484 (2021).
8. Hwang, S., Chen, X., Zhou, G. & Su, D. In situ transmission electron microscopy on energy-related catalysis. *Adv. Energy Mater.* **10**, 1902105 (2019).
9. Chen, M. et al. In-situ/operando Raman techniques for in-depth understanding on electrocatalysis. *Chem. Eng. J.* **461**, 141939 (2023).
10. Liu, H., Qi, Z. & Song, L. In situ electrocatalytic infrared spectroscopy for dynamic reactions. *J. Phys. Chem. C* **125**, 24289–24300 (2021).
11. Cullen, D. A. et al. New roads and challenges for fuel cells in heavy-duty transportation. *Nat. Energy* **6**, 462–474 (2021).
12. Lu, P. & Srinivasan, S. Advances in water electrolysis technology with emphasis on use of the solid polymer electrolyte. *J. Appl. Electrochem.* **9**, 269–283 (1979).
13. Lazaridis, T., Stühmeier, B. M., Gasteiger, H. A. & El-Sayed, H. A. Capabilities and limitations of rotating disk electrodes versus membrane electrode assemblies in the investigation of electrocatalysts. *Nat. Catal.* **5**, 363–373 (2022).

14. Seok, J. et al. La-based perovskite oxide catalysts for alkaline oxygen reduction: The importance of electrochemical stability. *J. Phys. Chem. C.* **126**, 3098–3108 (2022).
15. Zeng, R. et al. Nonprecious transition metal nitrides as efficient oxygen reduction electrocatalysts for alkaline fuel cells. *Sci. Adv.* **8**, eabj1584 (2022).
16. Wang, Y. et al. Synergistic Mn-Co catalyst outperforms Pt on high-rate oxygen reduction for alkaline polymer electrolyte fuel cells. *Nat. Commun.* **10**, 1506 (2019).
17. Jiao, K. et al. Designing the next generation of proton-exchange membrane fuel cells. *Nature* **595**, 361–369 (2021).
18. Lewis, E. A. et al. Operando X-ray absorption and infrared fuel cell spectroscopy. *Electrochim. Acta* **56**, 8827–8832 (2011).
19. Coz, E. et al. Water management in a planar air-breathing fuel cell array using operando neutron imaging. *J. Power Sources* **331**, 535–543 (2016).
20. Kim, J. et al. Structural insights into multi-metal spinel oxide nanoparticles for boosting oxygen reduction electrocatalysis. *Adv. Mater.* **34**, 2107868 (2021).
21. Yang, Y. et al. In situ X-ray absorption spectroscopy of a synergistic Co-Mn oxide catalyst for the oxygen reduction reaction. *J. Am. Chem. Soc.* **141**, 1463–1466 (2019).
22. Henke, B. L., Gullikson, E. M. & Davis, J. C. X-ray interactions: Photoabsorption, scattering, transmission, and reflection at $E=50\text{--}30,000\text{ eV}$, $Z=1\text{--}92$. *Atomic Data Nucl. Data Tables* **54**, 181–342 (1993).
23. Cueva, P., Hovden, R., Mundy, J. A., Xin, H. L. & Muller, D. A. Data processing for atomic resolution electron energy loss spectroscopy. *Microsc. Microanal.* **18**, 667–675 (2012).
24. Peng, H. et al. Alkaline polymer electrolyte fuel cells stably working at 80°C . *J. Power Sources* **390**, 165–167 (2018).
25. Ravel, B. & Newville, M. ATHENA, ARTEMIS, HEPHAESTUS: data analysis for X-ray absorption spectroscopy using IFEFFIT. *J. Synchrotron Radiat.* **12**, 537–541 (2005).
26. Kuo, C. H. et al. Facet-dependent catalytic activity of MnO electrocatalysts for oxygen reduction and oxygen evolution reactions. *Chem. Commun. (Camb.)* **51**, 5951–5954 (2015).

Acknowledgements

This work was supported by the Center for Alkaline Based Energy Solutions (CABES), part of the Energy Frontier Research Center (EFRC) program supported by the U.S. Department of Energy, under Grant DE-SC-0019445. This work made use TGA, XRD, and TEM of the Cornell Center for Materials Research Facilities supported by the National Science Foundation under Award Number DMR-1719875 and NSF-MRI-1429155. QL acknowledges support by the New York State Energy Research and Development Authority (NYSERDA) under agreement 146218. A.M.V. acknowledges support by the National Science Foundation (NSF) Graduate Research Fellowship Program (GRFP) grant DGE-1650441 and DGE-2139899, and the Cornell Dean's Excellence Scholarship. J.S. acknowledge support by the Cornell Energy Systems Institute (CESI) and the Kavli Institute at Cornell (KIC). This work is based on research conducted at the Center for High-Energy X-ray Sciences

(CHEXS), which is supported by the National Science Foundation (BIO, ENG and MPS Directorates) under award DMR-1829070. We thank the Cornell LASSP Professional Machine Shop for machining the in-situ and operando cells.

Author contributions

Q. L. conceived and designed the experiments and wrote the manuscript under the supervision of H. D. A. Q.L. synthesized the materials, conducted XRD, TGA, STEM, EELS characterizations, electrochemical measurements, and AEMFC tests. Z. S. assisted in STEM and EELS characterizations under the supervision of D.M. Q.L. carried out in-situ and operando XAS experiments with support from C. P., J. S., A. M. V., M. R. K., Z. S., and conducted data analysis. All authors participated in result discussions and manuscript review.

Competing interests

The authors declare no competing interests.

Additional information

Supplementary information The online version contains supplementary material available at <https://doi.org/10.1038/s41467-025-57177-y>.

Correspondence and requests for materials should be addressed to Héctor D. Abruña.

Peer review information *Nature Communications* thanks Nozomu Ishiguro and the other anonymous reviewer(s) for their contribution to the peer review of this work. A peer review file is available.

Reprints and permissions information is available at <http://www.nature.com/reprints>

Publisher's note Springer Nature remains neutral with regard to jurisdictional claims in published maps and institutional affiliations.

Open Access This article is licensed under a Creative Commons Attribution-NonCommercial-NoDerivatives 4.0 International License, which permits any non-commercial use, sharing, distribution and reproduction in any medium or format, as long as you give appropriate credit to the original author(s) and the source, provide a link to the Creative Commons licence, and indicate if you modified the licensed material. You do not have permission under this licence to share adapted material derived from this article or parts of it. The images or other third party material in this article are included in the article's Creative Commons licence, unless indicated otherwise in a credit line to the material. If material is not included in the article's Creative Commons licence and your intended use is not permitted by statutory regulation or exceeds the permitted use, you will need to obtain permission directly from the copyright holder. To view a copy of this licence, visit <http://creativecommons.org/licenses/by-nc-nd/4.0/>.

© The Author(s) 2025